



Design and Experimental Study of Wide-Speed-Range Morphing Waveriders with Fixed Leading-Edge and Windward-Surface Area

Yiqi Tang¹, Chongguang Shi², Xiaogang Zheng³, Yancheng You⁴

Abstract

Waveriders achieve superior aerodynamic performance through high lift-to-drag ratios and reduced thermal loads, positioning them as the preferred configuration for hypersonic vehicles. However, conventional fixed configurations reliant on single-point design suffer significant aerodynamic degradation in off-design conditions, limiting their applicability to wide-speed-range and large-flight-envelope scenarios. Consequently, morphing waveriders have emerged as a critical research frontier for future near-space hypersonic vehicles. To address this challenge, this paper proposes a novel methodology for designing wide-speed-range morphing waveriders featuring an invariant leading edge and constant windward surface area, accompanied by experimental validation of the designed configurations at Mach 5.0, 6.0, and 8.0. Experimental results demonstrate that the morphing waveriders maintain favourable wave-riding and lift-to-drag characteristics across the wide Mach range, with the maximum lift-to-drag ratio consistently exceeding 4.2. The influence of the angle of attack on the aerodynamic performance of the waverider is also investigated.

Keywords: Morphing Waveriders, Wide-speed-range, Hyper Sonic, Wind Tunnel Experiment

Nomenclature

uppercase letters

P – normalized pressure gradient

D – streamline curvature

 S_a – shock curvature in flow plane

 S_b – shock curvature in flow-normal plane

M – Mach number

H – altitude

S – windward area

 P_t – total pressure

 T_t – total temperature

Re - Reynolds number

 C_L – lift coefficient

 C_D – drag coefficient

 C_{My} – pitching moment coefficient

lowercase letters

w – semi-spanwise width of waverider

k − osculating plane scaling factor

p – static pressure

q – dynamic pressure

Greek symbols

√ - sweep angle

a – osculating plane angle

 δ – flow deflection angle

 θ – shock angle

subscripts

1 – pre-shock parameter

2 – post-shock parameter

0 – freestream parameter

superscripts

'- gradient of variables

1. Introduction

The waverider has become the preferred configuration for hypersonic vehicles due to its high lift-to-drag ratio [1-3], primarily attributed to the high-pressure flow confined beneath the windward surface by an attached leading-edge shock wave [4]. Since Nonweiler [5] pioneered the wedge-derived

¹ School of Aerospace Engineering, Xiamen University, China, <u>35020230156550@stu.xmu.edu.cn</u>

² School of Aerospace Engineering, Xiamen University, China, chongguangshi@xmu.edu.cn

³ School of Aerospace Engineering, Xiamen University, China, <u>xiaoqanqzhena@xmu.edu.cn</u>

⁴ School of Aerospace Engineering, Xiamen University, China, <u>vancheng.you@xmu.edu.cn</u> (Corresponding Author)

waverider concept based on the wedge flowfield in 1959, significant research efforts have advanced waverider designs [6]. Nevertheless, conventional approaches based on single-Mach number design suffer significant aerodynamic degradation under off-design conditions, constraining their applicability across wider airspace. Therefore, wide-speed-range waverider design has gradually become a hot topic of research [7]. Earlier a "combined" waverider formed by integrating high- and low-speed-derived configurations was developed to balance wide-speed-range performance. For instance, Wang et al. [8] put forward a tandem-configured vehicle aligned streamwise, while Li et al. [9] proposed a parallelconfigured vehicle arranged spanwise. Originating from the parallel-design idea [9], methodologies for variable-Mach-number waveriders have evolved. Zhang et al. [10] first designed a wide-speed-range vehicle by tracing streamlines in conical flowfields with different Mach numbers. To further enhance design flexibility, Zhao et al. [11] and Liu et al. [12] refined variable-Mach-number waverider designs on the basis of osculating cone and osculating flowfield theories, respectively. In addition, Rodi [13] created a novel category of vortex lift waveriders featuring constant or variable leading-edge sweep angles that generate strong vortices on the leeward surface. Zhao et al. [14] developed two kinds of design methods for constant-swept waveriders and analyzed the high-speed aerodynamic performance of cuspidal and delta-winged waveriders. Zhao et al. [15] made further investigations into the lowspeed aerodynamic performance of these waveriders, and concluded that the leading-edge vortex effect and shock effect are primary lift sources in low- and high-speed regimes, respectively. Recently, Sun et al. [16] proposed a reversible integrated configuration with distinct inlets on the upper and lower surfaces, enabling multi-point cruise through fuselage rotation.

Although the aforementioned waverider designs expand the flight speed range, such fixed-configuration designs are essentially compromise solutions that inherently restrict their aerodynamic and geometric performance to an acceptable balance. Consequently, morphing waveriders have emerged to optimize full-flight-envelope performance by addressing high- and low-speed conflicts, positioning them as a promising technology for future hypersonic vehicles. The concept of morphing waveriders dates back to 2003, when Bowcutt [17] designed a waverider incorporating variable leading-edge flaps to generate a continuum of optimal configurations across varying Mach numbers and flight attitudes. Liu et al. [18] developed a multistage morphing waverider featuring different conical-flow compression surfaces and presented two transfiguration flight strategies: application of smart materials and throwing of compression surfaces as cowlings. In 2016, Maxwell [19] discovered that conical waveriders maintain nearly constant stream surface area across Mach numbers, motivating shapeable-stream-surface designs for constant dynamic pressure and constant altitude. On this foundation, the Naval Research Laboratory developed NRL morphing waveriders with a constant leading edge and morphing lower stream surface [20-21]. Phoenix et al. [20] identified a control-point set that enable a Mach 10 waverider to deform efficiently down to Mach 5. Phoenix et al. [21] extended this work to 3D models with realistic system stiffness and geometric constraints that morph from Mach 5 to Mach 3.5. In addition to their conceptual validation, the application of NRL morphing waveriders to scramjet inlet manifolds and entry vehicles has been investigated [22-23]. Recently, Dai et al. [24] proposed a variable-sweep-wing morphing waverider, while Oiao et al. [25] introduced a reentry morphing waverider with rotating telescopic wings.

For more than sixty years since the conception of the waverider, validation of design methodologies and aerodynamic performance has predominantly depended on computational fluid dynamics (CFD). Nevertheless, essential wind-tunnel tests remain indispensable, as numerical simulation alone cannot fully verify methodological reliability or performance fidelity. Therefore, extensive experimental investigations focused on waverider configurations have been pursued [26-33]. Recently, to verify the potential advantages of double-swept waveriders over wide-speed range, Liu et al. performed several experimental studies, analyzing their on-design [34], off-design [35], and subsonic to supersonic performance [36]. Generally speaking, however, such studies remain notably scarce. More critically, to date, the design concepts and wide-speed-range performance of morphing waveriders have not yet been validated by wind-tunnel tests.

To address the aforementioned challenges, this work proposes a novel wide-speed-range morphing waverider concept featuring an invariant leading edge and constant windward surface area, supported by experimental validation of the designed configurations at Mach 5.0, 6.0, and 8.0. The remainder of this paper is structured as follows: Section 2 elaborates on the design methodology for wide-speed-range morphing waveriders; Section 3 describes the experimental setup, including the test facility and

models; Section 4 discusses the experimental results, analyzing the aerodynamic performance and flow characteristics of the proposed morphing waveriders; and Section 5 provides concluding remarks.

2. Design Methodology

The three-dimensional leading edge of the waverider directly relates to fundamental geometric characteristics such as sweep angle, dihedral angle, and volumetric efficiency, which further influence aerodynamic performance [37-39]. Thus, drawing on morphing strategies employing smart materials and structures (e.g., thermosensitive or retractable strut-driven flexible skin), a novel wide-speed-range morphing waverider concept has been proposed by incorporating the constraint of maintaining constant leading-edge geometry and windward area. The design methodology for morphing waveriders builds upon the aerodynamics-informed parametric (AIP) method developed in the authors' prior work [39]. The AIP method enables efficient waverider generation for varying design curves and accommodates curved shocks. Considering the aforementioned design constraints, we input an invariant leading-edge profile curve (LEPC) and adjust the shock wave to ensure constant windward area across all waverider configurations designed at distinct Mach numbers. The AIP method with LEPC input is briefly introduced below. Subsequently, we outline the design process for wide-speed-range morphing waveriders.

2.1. AIP method with LEPC input

As illustrated in Fig. 1, waverider design constrained by a specified LEPC requires shock wave determination and streamline solution. The analytical expression for the shock wave profile curve (SWPC) is derived from geometric relationships among design curves, followed by obtaining waverider streamline formulations based on curved shock theory. The three-dimensional LEPC is jointly defined by its projection in the *yoz* plane - the flow capture tube (FCT) - and its projection in the *xoy* plane - the planform profile curve (PPC) - as follows:

$$\begin{cases} z = f(y) \\ x = p(y) \end{cases} \quad y \in [-w, w], \tag{1}$$

where w represents the semi-spanwise width of waverider.

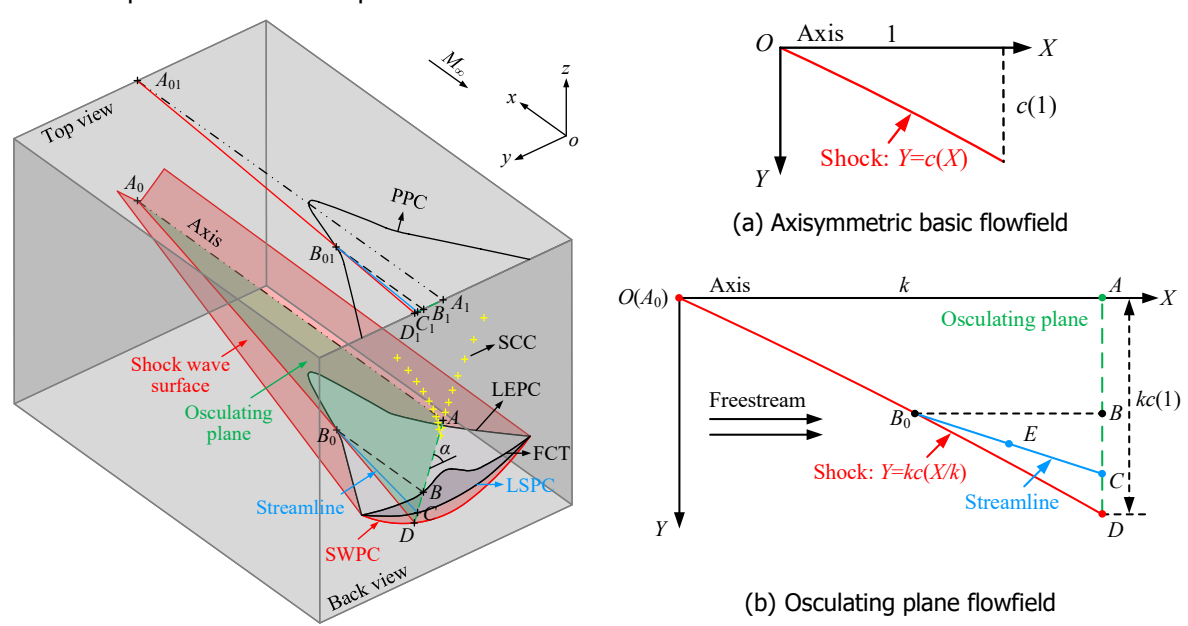


Fig 1. Schematic diagram of AIP method with LEPC input [39]

Fig 2. Geometric correlation in axisymmetric basic and osculating plane flowfields

Fig. 2(a) depicts the axisymmetric basic flowfield in the XOY plane, where the curved shock wave is governed by:

$$Y = c(X), \quad X \in [0,1].$$
 (2)

As shown in Fig. 2(b), the shock wave in the osculating plane is generated by geometrically scaling its

counterpart in the basic flowfield, satisfying the governing equation:

$$Y = kc(X/k), \quad X \in [0, k], \tag{3}$$

where k denotes the geometric scaling factor for the osculating plane.

As depicted in Fig. 3(a), the projection of any leading-edge point B_0 onto the base plane defines point B on the FCT, with the associated osculating plane intersecting the SWPC at shock point D. Crucially, the tangent to the LEPC at point B_0 intersects both the tangent to the FCT at point D and the tangent to the SWPC at point D at a common point D, with tangent segments D and D lying entirely within the base plane. The sweep angle D of LEPC at point D is calculated from

$$\lambda = 90^{\circ} - \arccos\left(\frac{\overline{B_0 F}}{\left|\overline{B_0 F}\right|} \bullet \frac{\overline{B_0 B}}{\left|\overline{B_0 B}\right|}\right) = 90^{\circ} - \arccos\left[\frac{p'(y_{B_0})}{\sqrt{\left(p'(y_{B_0})\right)^2 + 1 + \left(f'(y_{B_0})\right)^2}}\right]. \tag{4}$$

Fig. 3(b) illustrates the base plane design curves, where the angular relationship in triangle *BDF* is self-evident:

$$\alpha = \beta - \varphi + 90^{\circ}. \tag{5}$$

Here, the angle β between tangent segment BF and the horizontal direction, and the angle φ between tangent segments BF and DF, are computed by

$$\beta = \arctan \left[f' \left(\gamma_{\beta_0} \right) \right], \tag{6}$$

and

$$\varphi = \arcsin\left(\frac{|BD|}{|BF|}\right) = \arcsin\left(\frac{Y_D - Y_{B_0}}{|B_0B|/\tan(\lambda)}\right) = \arcsin\left(\frac{k\left[c\left(1\right) - c\left(1 - X_{B_0}/k\right)\right]}{X_{B_0}/\tan(\lambda)}\right). \tag{7}$$

The position of shock point D is thus determined by the osculating plane angle a and the distance between points B and D, expressed as:

$$\begin{cases} y_D = y_{B_0} - |BD| \cos(\alpha), \\ Z_D = Z_{B_0} - |BD| \sin(\alpha). \end{cases}$$
 (8)

Substituting Eqs. 1-7 into Eq. 8 yields the analytical expression for SWPC under the prescribed *k*-distribution:

$$\begin{bmatrix}
y_{D} = y_{B_{0}} + k \left\{ c(1) - c \left[1 - \frac{p(y_{B_{0}})}{k} \right] \right\} \sin \left\{ \operatorname{arctan} \left[f'(y_{B_{0}}) \right] - \operatorname{arcsin} \left\{ \frac{k \left\{ c(1) - c \left[1 - \frac{p(y_{B_{0}})}{k} \right] \right\} \right\}}{\frac{p(y_{B_{0}})}{p'(y_{B_{0}})} \sqrt{1 + \left(f'(y_{B_{0}}) \right)^{2}}} \right\} \right\}, \\
z_{D} = f(y_{B_{0}}) - k \left\{ c(1) - c \left[1 - \frac{p(y_{B_{0}})}{k} \right] \right\} \cos \left\{ \operatorname{arctan} \left[f'(y_{B_{0}}) \right] - \operatorname{arcsin} \left\{ \frac{k \left\{ c(1) - c \left[1 - \frac{p(y_{B_{0}})}{k} \right] \right\} \right\}}{\frac{p(y_{B_{0}})}{p'(y_{B_{0}})} \sqrt{1 + \left(f'(y_{B_{0}}) \right)^{2}}} \right\} \right\}, \\
(9)$$

where f(y), p(y), and c(y) are design inputs, while (y_D, z_D) are design outputs. By repeating the above procedure along the LEPC (i.e., varying y_{E0} within [-w, w]), the SWPC is obtained.

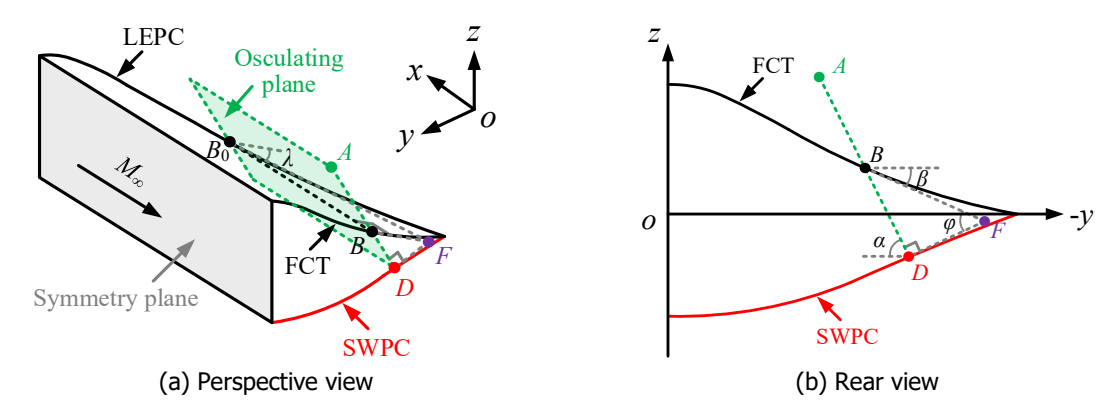


Fig 3. Geometric relationships between design curves from perspective and rear views

Given freestream conditions, post-shock flow parameters and their first- and second-order derivatives are determined through the sequential application of oblique shock wave relations, first-order curved shock equations [40]

$$\begin{cases}
A_1P_1 + B_1D_1 + E_1\Gamma_1 = A_2P_2 + B_2D_2 + CS_a + GS_b, \\
A_1P_1 + B_1D_1 + E_1\Gamma_1 = A_2P_2 + B_2D_2 + CS_a + GS_b,
\end{cases} (10)$$

and second-order curved shock equations [41]

$$\begin{cases} A_{1}^{"}P_{1}' + B_{1}^{"}D_{1}' + E_{1}^{"}\Gamma_{1}' = A_{2}^{"}P_{2}' + B_{2}^{"}D_{2}' + C^{"}S_{a}' + G^{"}S_{b}' + \text{const.}'', \\ A_{1}^{"}P_{1}' + B_{1}^{"}D_{1}' + E_{1}^{"}\Gamma_{1}' = A_{2}^{"}P_{2}' + B_{2}^{"}D_{2}' + C^{"}S_{a}' + G^{"}S_{b}' + \text{const.}'''. \end{cases}$$

$$(11)$$

The variables and their gradients in Eqs. 10 and 11 are defined as:

normalized pressure gradient:
$$P = (\partial p/\partial s)/\rho V^2$$
, streamline curvature: $D = \partial \delta/\partial s$, normalized vorticity: $\Gamma = \omega/V$, shock curvature: $S_a = \partial \theta/\partial \sigma$, $S_b = -\cos\theta/Y$, normalized second-order pressure gradient: $P' = (\partial^2 p/\partial s^2)/\rho V^2$, streamline curvature gradient: $D' = \partial^2 \delta/\partial s^2$, normalized vorticity gradient: $\Gamma' = \partial \Gamma/\partial \sigma$, shock curvature gradient: $S_a' = \partial S_a/\partial \sigma$, $S_b' = \partial S_b/\partial \sigma$,

where p, ρ , V, δ , ω , and θ denote pressure, density, velocity, deflection angle, vorticity, and shock angle, respectively. Coefficients are calculable from freestream conditions and shock angle (detailed in Refs. 40 and 41). Subscripts 1 and 2 designate pre- and post-shock flow parameters.

Building on this foundation and incorporating the assumption that P and D remain constant along streamlines, post-shock streamlines can be traced using Taylor series expansion. For instance, as illustrated in Fig. 2(b), once shock A_0D and point B_0 are determined, the post-shock streamline B_0C within the osculating plane A_0AD is drawn by

$$Y = Y_{B_0} + \left(X - X_{B_0}\right) \frac{dY}{dX} + \frac{\left(X - X_{B_0}\right)^2}{2} \frac{d^2Y}{dX^2} + \frac{\left(X - X_{B_0}\right)^3}{6} \frac{d^3Y}{dX^3} + ...,$$
(13)

where

$$\frac{dY}{dX} = \tan \delta_{B_0}, \quad \frac{d^2Y}{dX^2} = \frac{D_0}{\cos^3 \delta_{B_0}}, \quad \frac{d^3Y}{dX^3} = \frac{3D_{B_0}^2 \tan \delta_{B_0} + D_{B_0}'}{\cos^4 \delta_{B_0}}.$$
 (14)

Furthermore, via geometric transformation relations, the Cartesian coordinates of any point on streamline B_0C , such as point $E(x_E, y_E, z_E)$, are derived as:

HiSST-2025-0219 Page | 5
Design and experimental study of wide-speed-range morphing waveriders with fixed leading-edge and windward-surface area
Copyright © 2025 by author(s)

$$\begin{cases} X_{E} = X_{B_{0}} - \Delta X, \\ Y_{E} = Y_{B_{0}} - \left[\Delta x \tan \delta_{B_{0}} + \frac{(\Delta x)^{2}}{2} \frac{D_{B_{0}}}{\cos^{3} \delta_{B_{0}}} + \frac{(\Delta x)^{3}}{6} \frac{3D_{B_{0}}^{2} \tan \delta_{B_{0}} + D_{B_{0}}'}{\cos^{4} \delta_{B_{0}}} \right] \cos \alpha, \\ Z_{E} = Z_{B_{0}} - \left[\Delta x \tan \delta_{B_{0}} + \frac{(\Delta x)^{2}}{2} \frac{D_{B_{0}}}{\cos^{3} \delta_{B_{0}}} + \frac{(\Delta x)^{3}}{6} \frac{3D_{B_{0}}^{2} \tan \delta_{B_{0}} + D_{B_{0}}'}{\cos^{4} \delta_{B_{0}}} \right] \sin \alpha, \end{cases}$$
(15)

where varies from 0 to x_{80} . Repeating this procedure along the LEPC (i.e., varying y_D within [-w, w]) and integrating streamlines across all osculating plane forms the complete waverider windward surface, with its exit profile constituting the LSPC in Fig. 1. Detailed derivations of other flow parameters are provided in Ref. 39.

2.2. Design process for wide-speed-range morphing waveriders

Fig. 4 schematizes the design flowchart for wide-speed-range morphing waveriders. The design process is implemented as follows: First, input the Mach number range $[M_1, M_2]$ based on the flight envelope, and specify the design Mach number (M) and corresponding altitude (H) for each target phase. Second, invoke the AIP method module iteratively to generate the windward surfaces of multi-stage waveriders with invariant leading-edge geometry and constant area. Third, construct the upper surfaces as identical freestream configurations and assemble them with the windward surfaces into complete waveriders. Finally, analyze the aerodynamic and volumetric performance of the waveriders. If these performance metrics meet the requirements, output the wide-speed-range morphing waveriders. Otherwise, return to the second step and input a new leading edge.

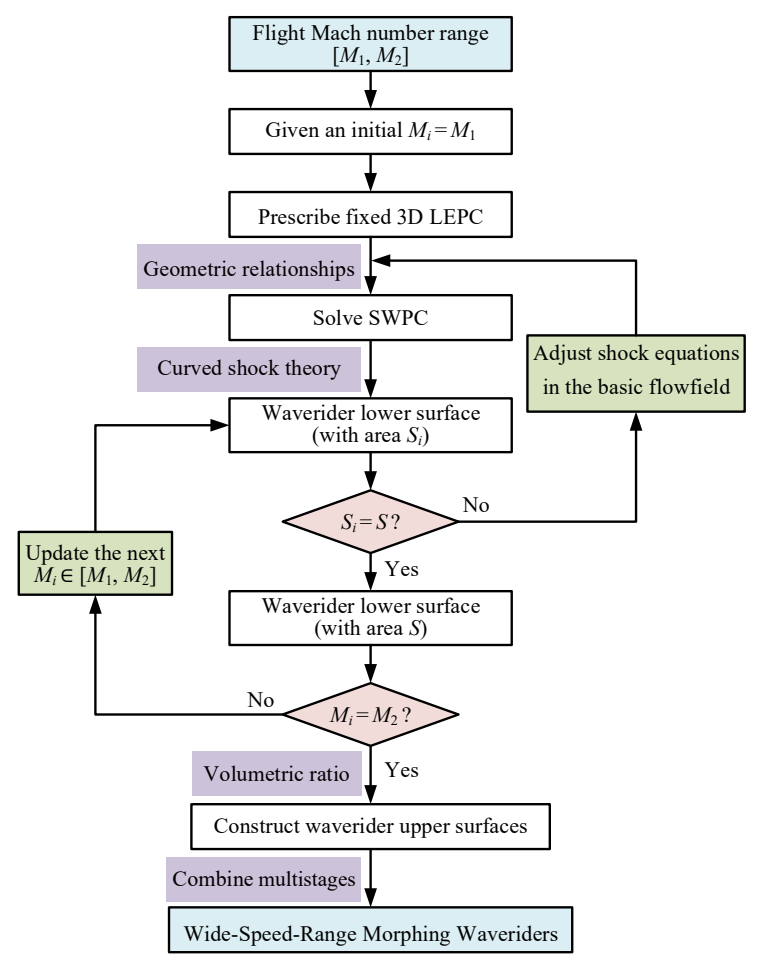


Fig 4. Flowchart of wide-speed-range morphing waverider design using the AIP method

Now, we proceed to detail the procedure for the second step, beginning with the first invocation of the AIP method module (i.e., $M_i = M_1$). First, define a leading edge (Eq. 1) that satisfies geometric

constraints, such as the slenderness ratio and dihedral angle. Then, prescribe the curved shock wave (Eq. 2) in the axisymmetric basic flowfield. Subsequently, derive the analytical shock surface (Eq. 9) based on geometric relationships between design curves (Eqs. 3-8). Finally, employ curved shock theory (Eqs. 10 and 11) to obtain analytical streamlines (Eq. 13), and integrate them to generate the analytical waverider windward surface (Eq. 15). Following this, check if the current windward surface area S_i equals the target area S_i . If not, adjust the basic shock equation and reinvoke the AIP method module. If equal, verify whether the current design Mach number M_i matches the terminal Mach number M_2 . If not, update to the next Mach number $M_i \in [M_1, M_2]$, adjust the basic shock equation, and reinvoke the AIP method module. If equal, proceed to the third step.

3. Experimental Setup

Employing the design methodology under wind tunnel operability constraints, Mach 5.0, 6.0, and 8.0 were strategically selected as pivotal design nodes for the development of wide-speed-range morphing waveriders. As shown in Fig. 5, the wind tunnel models share identical leading-edge geometry with a total length of 400.6 mm, wingspan of 223.3 mm, and aspect ratio of 1.8. The windward-surface area of these three models, which serves as the reference area for normalizing aerodynamic coefficients in subsequent analyses, measures 0.027 m². An increase in the design Mach number leads to progressively enhanced convexity of the waverider's windward surface. The upper surfaces are designed to remain parallel to the freestream direction. To ensure the credibility of the experimental data, model dimensions were strictly controlled to avoid the choking phenomenon. However, the ideal waverider configurations generated using the design method incorporate a sharp leading edge, which is impractical for manufacturing. To address this, the blunting technique was adopted to modify the leading edge, achieving a blunt radius of 0.53 mm by elevating the upper surface. The models were machined from 30CrMnSiA alloy structural steel, and a support rod coated with thermal insulation ceramic spray was used to install a TG618 six-component sting balance.







Fig 5. Wide-speed-range morphing waverider models for wind tunnel experiments

The experiments were conducted in the FD-07 hypersonic wind tunnel at China Academy of Aerospace Aerodynamics. This intermittent blowdown facility operates with air as the working medium and features an interchangeable nozzle with an exit diameter of 500 mm, providing nominal freestream Mach numbers from 4.0 to 8.0. The effective test duration is approximately 60 to 120 seconds. For operations above Mach 6, the nozzle is equipped with a water-cooling system to prevent thermal deformation of critical components. The test platform features a four-degree-of-freedom rapid insertion mechanism, enabling precise angle-of-attack adjustments from -10° to 50° during testing. The free-jet test section with an enclosed chamber measures 1880 mm \times 1400 mm \times 1130 mm and is fitted with two opposing optical-grade glass windows, each with a clear aperture of 520 mm \times 320 mm, on the lateral walls for model inspection and schlieren-based flow visualization. Only Mach and Reynolds numbers were simulated in the experiment, without considering the impact of turbulent intensity.

The experimental Mach numbers were 4.937, 5.933, and 7.948, respectively, with flow conditions detailed in Table 1. The nomenclature is as follows: P_t denotes total pressure, T_t corresponds to total temperature, Re designates freestream Reynolds number per unit length, and dynamic and static pressures are represented by q_0 and p_0 , respectively. Force measurement tests were conducted on the M5, M6, and M8 configurations across 11 angle-of-attack (AOA) conditions (-4° to 4°, 6°, and 8°), 11 AOA conditions (-4° to 6°), and 8 AOA conditions (-4°, -2°, 0° to 5°), respectively. For comparative validation, viscous CFD simulations were performed under identical conditions.

М	P _t (Mpa)	T _t (°C)	q ₀ (Mpa)	p ₀ (pa)	Re (1/m)	AOA (°)
4.937	1	90	0.036	2100	2.12 ×107	-4~4, 6, 8
5.933	2	191	0.033	1360	1.87 ×107	-4~6
7.948	5	475	0.023	524	1.10 ×107	-4, -2, 0~5

Table 1. Experimental states in hypersonic wind tunnel

4. Results and Discussion

4.1. Shock wave location and shape

Consider now the on- and off-design aerodynamic performance of the waverider models under varying AOA. Fig. 6 presents a sequence of side-view color schlieren photographs of the three models at Mach 4.937, 5.933, and 7.948. For conciseness, only AOA cases of -4°, 0°, and 4° are displayed. These images clearly resolved two distinct shock structures: the upper- and lower-surface leading-edge shock waves, confirming that the designed waveriders maintained desirable wave-riding performance. The upper-surface shock wave was induced by the blunt leading edge and viscous boundary layer, while the lower-surface shock wave comprised compression waves generated by the waverider lower surface with a curvature gradient.

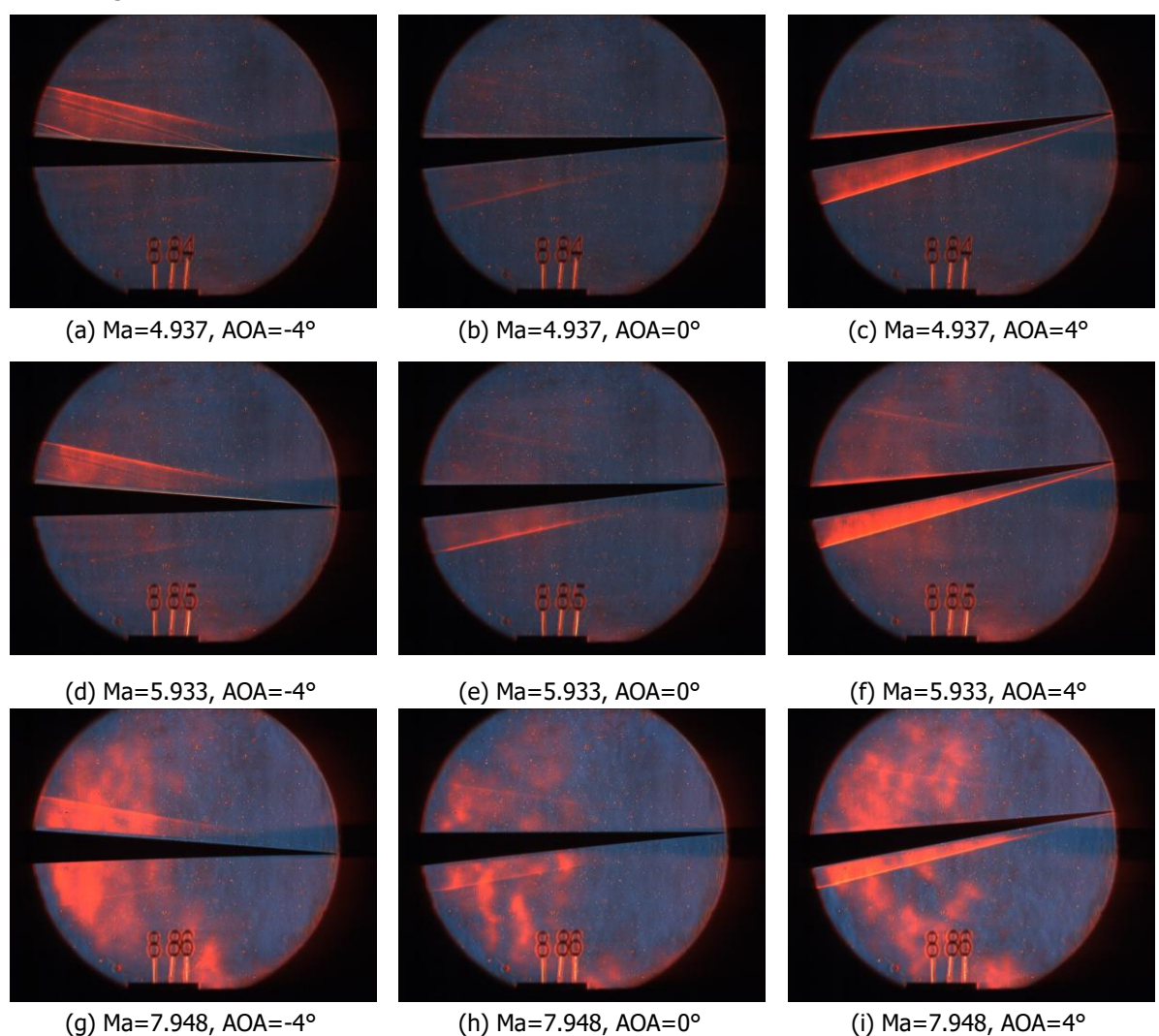


Fig 6. Schlieren photographs in the symmetry plane of the experimental models

The influence of AOA on both shock waves is consistent among all three configurations. Taking the M5 configuration as an example, as shown in Figs. 6(a) and 6(b), negative AOA variations significantly

intensify the upper-surface shock wave, while the lower-surface shock wave maintains relatively stable positional and morphological characteristics during AOA reduction. Conversely, a comparison between Figs. 6(b) and 6(c) shows minor differences in the upper-surface shock wave, indicating a limited influence of positive AOA variations on flow structures around the waverider's nose region and upper surface. In contrast, the position and morphology of the lower-surface shock wave exhibit more pronounced variations as the AOA increases, with the shock progressively approaching the wall. In addition, as the AOA increases, the color of the lower-surface shock wave gradually deepens, and the shock layer thickens, demonstrating enhanced shock intensity.

4.2. Aerodynamic performance at varying angles of attack

Fig. 7 presents the dimensionless aerodynamic characteristics of the wide-speed-range morphing waverider models under variable AOA, where curves denote CFD simulations and discrete markers represent experimental measurements. The CFD predictions demonstrate strong congruence with experimental measurements across the tested AOA range. As shown in Fig. 7(a), the morphing waveriders maintain favorable lift-to-drag characteristics over the wide speed range. With increasing AOA, all configurations display an initial increase followed by a decrease in L/D ratios. Maximum L/D ratios exceed 4.2 at their respective design Mach numbers: the M5 configuration achieves 5.12 at AOA=4°, M6 reaches 4.75 at AOA=3°, and M8 attains 4.29 at AOA=3°. When the AOA exceeds 3°, the performance degradations remain moderate. Notably, the M5 and M8 configurations outperform the M6 configuration under positive and negative AOA conditions, respectively. Figs. 7(b)-(d) reveal that lift coefficient (C) and pitching moment coefficient (C) demonstrate near-linear proportionality to AOA, while drag coefficient (C) first decreases and then increases. Under positive AOA, the divergence in growth rates between C and C explains the non-monotonic C trend (initial rise followed by decline). Conversely, under negative AOA, C continues to increase whereas C decreases monotonically, resulting in an ascending C trend throughout this regime.

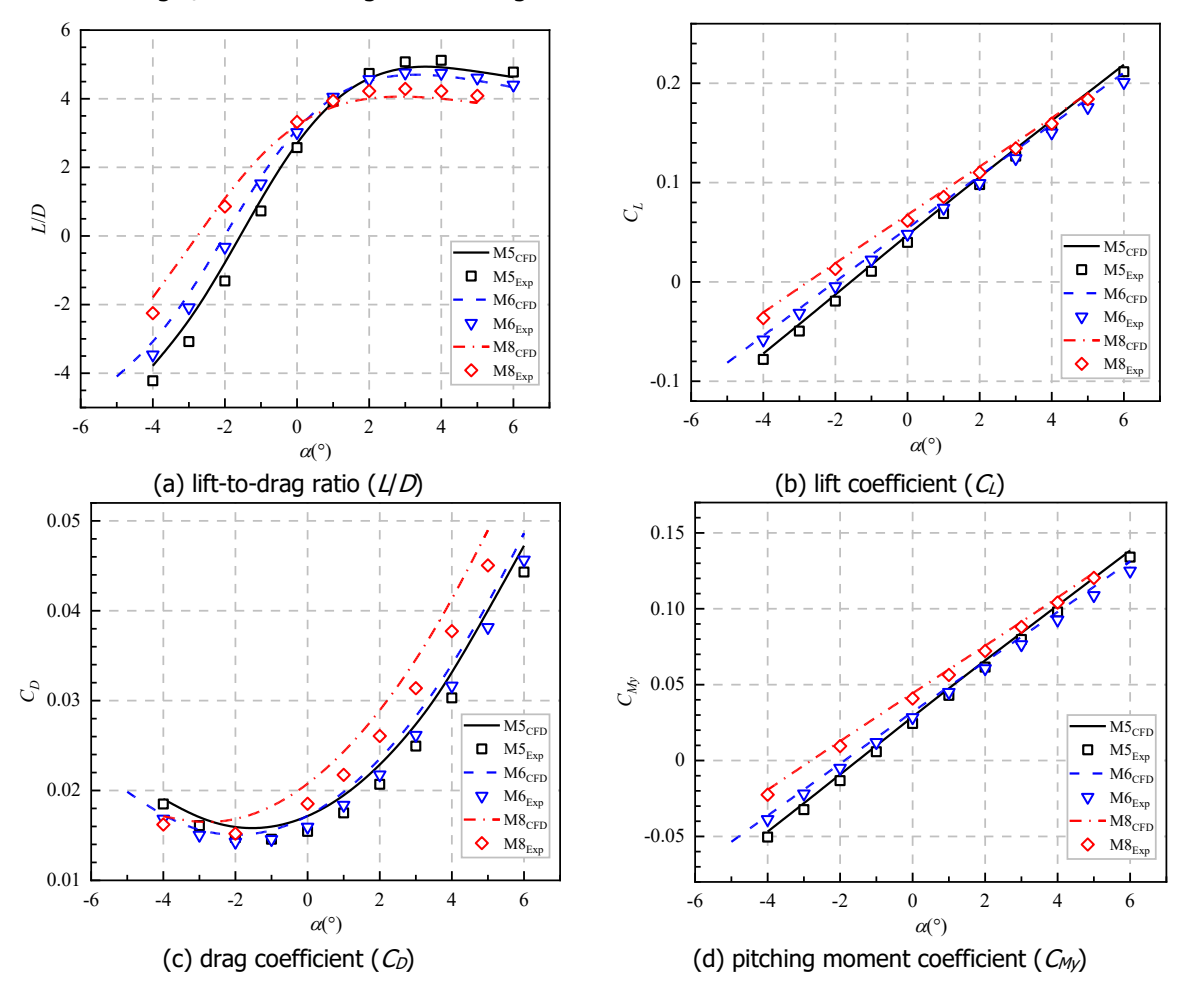


Fig 7. Comparison of aerodynamic performance between CFD and wind tunnel experiment (EXP)

Furthermore, Figs. 7(b) and 7(c) reveal that at high AOA, the C_L of all configurations exhibit minimal variation, whereas the C_D of the M8 waverider significantly exceeds those of the M5 and M6 configurations. This disparity accounts for the relatively inferior L/D characteristics of the M8 configuration under high AOA conditions. In contrast, the M5 configuration demonstrates higher C_L and lower C_D compared to the M6 counterpart at elevated AOA, resulting in superior L/D performance for the M5 variant under these conditions.

5. Conclusion

In this study, a novel design methodology for wide-speed-range morphing waveriders with a fixed leading edge and constant windward-surface area is proposed and experimentally validated. Morphing waverider models for Mach 5, 6, and 8 were designed and manufactured, with force and moment measurements conducted using a six-degree-of-freedom sting balance. Schlieren visualization confirmed that the waveriders maintain stable shock-attachment characteristics across the targeted Mach regime. Experimental results demonstrate excellent agreement with computational fluid dynamics simulations. The morphing waveriders exhibit favorable lift-to-drag performance throughout the speed range, with maximum lift-to-drag ratios exceeding 4.2 at their respective design Mach numbers. For all configurations, as the angle of attack increases, the lift-to-drag ratio initially rises and then declines; the lift and pitching moment coefficients show an approximately linear relationship, while the drag coefficient first decreases and then increases. Notably, the M5 configuration outperforms the others at positive angles of attack, whereas the M8 configuration shows superior performance at negative angles. Overall, the proposed approach broadens the design concepts for wide-speed-range morphing waveriders and promotes their engineering application. Future work will focus on multidisciplinary optimization of the morphing waverider design.

References

- 1. Walker SH, Rodgers F. Falcon hypersonic technology overview. 13th International Space Planes and Hypersonics Systems and Technologies; Capua, Italy. Reston: AIAA; 2005. p. 3253.
- 2. Hank JM, Murphy JS, Mutzman RC. The X-51A scramjet engine flight demonstration program. 15th AIAA International Space Planes and Hypersonic Systems and Technologies Conference; Dayton, Ohio, USA. Reston: AIAA; 2008. p. 2540.
- 3. Lunan DA. Waverider, a revised chronology. 20th AIAA International Space Planes and Hypersonic Systems and Technologies Conference; Glasgow, Scotland. Reston: AIAA; 2015. p. 3529.
- Küchemann D. The aerodynamic design of aircraft. Oxford: Pergamon Press; 1978. p. 448-510.
- 5. Nonweiler TRF. Aerodynamic problems of manned space vehicles. J R Aeronaut Soc 1959;63(585):521-8.
- 6. Ding F, Liu J, Shen CB, et al. An overview of research on waverider design methodology. Acta Astronaut 2017;140:190-205.
- 7. Zhao ZT, Huang W, Yan L, et al. An overview of research on wide-speed range waverider configuration. Prog Aerosp Sci 2020;113:100606.
- 8. Wang FM, Ding HH, Lei MF. Aerodynamic characteristics research on wide-speed range waverider configuration. Sci China Ser E-Technol Sci 2009;52(10):2903–10.
- 9. Li SB, Huang W, Wang ZG, et al. Design and aerodynamic investigation of a parallel vehicle on a wide-speed range. Sci China Inf Sci 2014;57:1–10.
- 10. Zhang TT, Wang ZG, Huang W, et al. A design approach of wide-speed-range vehicles based on the cone-derived theory. Aero Sci Technol 2017;71:42–51.
- 11. Zhao ZT, Huang W, Li SB, et al. Variable Mach number design approach for a parallel waverider with a wide-speed range based on the osculating cone theory. Acta Astronaut 2018;147:163–74.

- 12. Liu J, Liu Z, Wen X, et al. Novel osculating flowfield methodology for wide-speed range waverider vehicles across variable Mach number. Acta Astronaut 2019;162:160–7.
- 13. Rodi PE. Vortex lift waverider configurations. 50th AIAA Aerospace Sciences Meeting including the New Horizons Forum and Aerospace Exposition; Nashville, Tennessee, USA. Reston: AIAA; 2012. p. 1238.
- 14. Zhao ZT, Huang W, Yan BB, et al. Design and high speed aerodynamic performance analysis of vortex lift waverider with a wide-speed range. Acta Astronaut 2018;151:848-63.
- 15. Zhao ZT, Huang W, Yan L, et al. Low speed aerodynamic performance analysis of vortex lift waveriders with a wide-speed range. Acta Astronaut 2019;161:209–21.
- 16. Sun YH, Luo SB, Liu J, et al. Aerodynamic configuration of a wide-range reversible vehicle. Chin J Aeronaut 2025;38(4):103254.
- 17. Bowcutt KG, inventor; The Boeing Company, assignee. Hypersonic waverider variable leading edge flaps. United States patent US 6634594 B1. 2003 Oct 21.
- 18. Liu Z, Liu J, Ding F, et al. Novel methodology for wide-ranged multistage morphing waverider based on conical theory. Acta Astronaut 2017;140:362–9.
- 19. Maxwell JR. Hypersonic waverider stream surface actuation for variable design point operation. 52nd AIAA/SAE/ASEE Joint Propulsion Conference; Salt Lake City, UT, USA. Reston: AIAA; 2016. p. 4706.
- 20. Maxwell JR, Goodwin GB. Shapeable inlet manifold for hypersonic scramjet. 55th AIAA aerospace sciences meeting; Grapevine, TX, USA. Reston: AIAA; 2017. p. 1385.
- 21. Maxwell JR. Shapeable hypersonic waverider entry vehicles. 53rd AIAA/SAE/ASEE joint propulsion conference; Atlanta, GA, USA. Reston: AIAA; 2017. p. 4880.
- 22. Phoenix AA, Rogers RE, Maxwell JR, et al. Mach five to ten morphing waverider: control point study. J Aircr 2019;56(2):493-504.
- 23. Phoenix AA, Maxwell JR, Rogers RE. Mach 5-3.5 morphing waverider accuracy and aerodynamic performance evaluation. J Aircr 2019;56(5):2047-61.
- 24. Dai P, Yan BB, Huang W, et al. Design and aerodynamic performance analysis of a variable-sweep-wing morphing waverider. Aero Sci Technol 2020;98:105703.
- 25. Qiao NX, Ma TL, Jing B, et al. Design and aerodynamic analysis of the morphing waverider with rotating telescopic wing for wide-speed-range flight. Aero Sci Technol 2025;158:109941.
- 26. Rasmussen ML, Jischke MC, Daniel DC. Experimental forces and moments on cone-derived waveriders for $M\infty = 3$ to 5. J Spacecr Rockets 1982;19(6):592-8.
- 27. Jischke MC, Rasmussen ML, Daniel DC. Experimental surface pressures on cone-derived waveriders for M∞ = 3-5. J Spacecr Rockets 1983;20(6):539-45.
- 28. Pegg RJ, Hahne DE, Cockrell CE. Low-speed wind tunnel tests of two waverider configuration models. Sixth International Aerospace Planes and Hypersonics Technologies Conference; Chattanooga, TN, USA. Reston: AIAA; 1995. p. 6093.
- 29. Cockrell CE, Huebner LD, Finley DB. Aerodynamic performance and flow-field characteristics of two waverider-derived hypersonic cruise configurations. 33rd Aerospace Sciences Meeting and Exhibit; Reno, NV, USA. Reston: AIAA; 1995. p. 0736.
- 30. Liu JX, Hou ZX, Chen XQ, et al. Experimental and numerical study on the aero-heating characteristics of blunted waverider. Appl Therm Eng 2013;51:301-14.
- 31. Pisano A, Whitfield C. Characterization of a hypersonic waverider in low-speed flight. AIAA Scitech 2024 Forum; Orlando, FL, USA. Reston: AIAA; 2024. p. 2330.

- 32. Miller RW, Argrow BM, Center KB, et al., Experimental verification of the osculating cones method for two waverider forebodies at Mach 4 and 6. 36th AIAA Aerospace Sciences Meeting and Exhibit; Reno, NV, USA. Reston: AIAA; 1998. p. 0682.
- 33. Lobbia MA, Suzuki K. Experimental investigation of a Mach 3.5 waverider designed using computational fluid dynamics. AIAA J 2014;53(6):1590-1601.
- 34. Liu CZ, Meng XF, Liu RJ, et al. Experimental and numerical investigation for hypersonic performance of double swept waverider. Acta Astronaut 2022;200:291-300.
- 35. Liu CZ, Liu RJ, Meng XF, et al. Experimental investigation on off-design performances of double-swept waverider. AIAA J 2023;61(4):1596-1607.
- 36. Liu CZ, Meng XF, Liu JZ, et al. Experimental investigation for subsonic, transonic, and supersonic performances of double-swept waverider. AIAA J 2023;61(10):4247-58.
- 37. Li ZH, Jiang CW, Hu SY, et al. Leading-edge cone method for waverider design. AIAA J 2023;61(6):2331-46.
- 38. Li ZH, Jiang CW, Hu SY, et al. Variable leading-edge cone method for waverider design. Chin J Aeronaut 2025;38(3):103225.
- 39. Tang YQ, Zheng XG, Shi CG, et al. Aerodynamics-informed parametric method for rapid waverider design based on the second-order curved shock theory. Chin J Aeronaut 2025;X:xxxxxx.
- 40. Mölder S. Curved shock theory. Shock Waves 2016;26(4):337-53.
- 41. Shi CG, Han WQ, Deiterding R, et al. Second-order curved shock theory. J Fluid Mech 2020;891:A21.